photonics

Article

Design and Analysis of Optomechanical Micro-Gyroscope for Angular-Vibration Detection

Jamal N. A. Hassan *, Wenyi Huang, Xing Yan, Senyu Zhang, Dingwei Chen, Guangjun Wen and Yongjun Huang *

School of Information and Communication Engineering, Sichuan Provincial Engineering Research, Center of Communication Technology for Intelligent IoT, University of Electronic Science and Technology of China, Chengdu 611731, China; wgj@uestc.edu.cn (G.W.)

* Correspondence: jamal1almelhany@gmail.com (J.N.A.H.); yongjunh@uestc.edu.cn (Y.H.)

Abstract: Micro-gyroscopes based on the Coriolis principle are widely employed in inertial navigation, motion control, and vibration analysis applications. Conventional micro-gyroscopes often exhibit limitations, including elevated noise levels and suboptimal performance metrics. Conversely, the advent of cavity optomechanical system technology heralds an innovative approach to micro-gyroscope development. This method enhances the device's capabilities, offering elevated sensitivity, augmented precision, and superior resolution. This paper presents our main contributions which include a novel dual-frame optomechanical gyroscope, a unique photonic crystal cavity design, and advanced numerical simulation and optimization methods. The proposed design utilizes an optical cavity formed between dual oscillating frames, whereby input rotation induces a measurable phase shift via optomechanical coupling. Actuation of the frames is achieved electrostatically via an interdigitated comb-drive design. Through theoretical modeling based on cavity optomechanics and finite element simulation, the operating principle and performance parameters are evaluated in detail. The results indicate an expected angular rate sensitivity of 22.8 mV/°/s and an angle random walk of 7.1×10^{-5} °/h$^{1/2}$, representing superior precision to existing micro-electromechanical systems gyroscopes of comparable scale. Detailed analysis of the optomechanical transduction mechanism suggests this dual-frame approach could enable angular vibration detection with resolution exceeding state-of-the-art solutions.

Keywords: micro-gyroscopes; optomechanical; photonic crystal; angular vibration; dual-frame

check for updates

Citation: Hassan, J.N.A.; Huang, W.; Yan, X.; Zhang, S.; Chen, D.; Wen, G.; Huang, Y. Design and Analysis of Optomechanical Micro-Gyroscope for Angular-Vibration Detection. *Photonics* **2024**, *11*, 186. https://doi.org/10.3390/photonics11020186

Received: 6 October 2023
Revised: 13 November 2023
Accepted: 31 December 2023
Published: 18 February 2024

1. Introduction

The gyroscope, as a kind of inertial sensor that can measure angular velocity and angular vibration, has wide-ranging applications in aerospace, industrial automation, and structural health monitoring where rotational or angular motion must be precisely tracked [1–3]. Over recent decades, micro-electromechanical systems (MEMS) gyroscopes leveraging the Coriolis effect have become particularly prevalent due to the ability to miniaturize sensitive elements using microfabrication techniques. Based on their structural configuration, MEMS gyroscopes typically fall into one of several categories, including framed resonators, vibrating beams or loops, and ring resonators [4–7]. Within the framed designs, single, double, and multi-mass block implementations have been developed to modulate the Coriolis forces [8–11]. We narrowed down the specific problem or gap that the study aims to address, such as the limitations of traditional MEMS gyroscopes that rely on electronic transduction and noise sources. Effects such as thermal fluctuations, material stresses, and electromagnetic interference (EMI) introduce uncertainties that constrain achievable measurement sensitivity and accuracy levels [12].

While MEMS sensors effectively enable linear vibration monitoring, conventional MEMS gyroscopes have seen limited application in angular vibration measurement due to typical resolutions in the order of microradians [13–16]. However, recent advances integrating micro-opto-electromechanical systems (MOEMS) have prompted new gyroscopic designs capable of pushing these boundaries. Specifically, optomechanical systems leveraging cavity-enhanced transduction have emerged as a versatile tool for sensing myriad physical quantities including displacement, mass, acceleration, and gravitational waves at micro/nano scales [17–22]. Notably, the Coriolis effect intrinsic to gyroscopic sensing allows the input of angular vibrations to modulate an optomechanical cavity, translating rotations into detectable changes in optical properties. This characteristic provides a conceptual basis for establishing a novel class of high-precision gyroscopes optimized for angular vibration detection [23–25]. However, prior works in this domain have focused primarily on theoretical descriptions, leaving a need for concrete device architectures capable of experimentally validating the potential of this sensing modality. The current study aims to address this gap by proposing and numerically characterizing a dual-mass optomechanical gyroscope design, establishing a pathway toward next-generation inertial sensors affording resolutions surpassing state-of-the-art MEMS solutions.

In this paper, a novel dual-frame optomechanical gyroscope architecture utilizing a photonic crystal cavity is presented. Through rigorous theoretical analysis grounded in optomechanical coupling principles, the detailed operating mechanism and transduction processes of the proposed design are elucidated. Complimenting this, finite element modeling is employed to numerically characterize both the mechanical behavior of the sensing element as well as the optical properties emerging from the photonic crystal structure. By leveraging simulations, key figures of merit, such as the scale factor relating output signals to input rotations and the fundamental noise floor limitations are computationally predicted. These performance metrics indicate the potential for this optomechanical gyroscope design to achieve angular resolutions surpassing existing MEMS-based solutions when implemented in an experimental setting. More broadly, the presented analyses establish a conceptual and analytical framework for future efforts to optimize optomechanical inertial sensors targeting high-precision angular vibration measurement. With further refinement, this dual-frame approach may ultimately fulfill the long-sought goal of inertial sensors integrating microscale form factors with nanoradian-level angular sensitivity.

2. Operation Principle

2.1. Dual-Frame Optomechanical Gyroscope Architecture Design

The proposed dual-frame optomechanical gyroscope design consists of three primary components as depicted in Figure 1a: an actuation element, a sensing element, and a detection module. First, the actuation element utilizes an electrostatic comb drive structure to induce resonance in the outer mass block ($m_x = m_2 + m_1$) via electrostatic pull-off forces. The sensing element comprises a central mass block ($m_y = m_1$) suspended by straight and U-shaped flexural beams. The straight beams connect the outer block to the substrate, while the U-shaped beams tether it to the central block. Critically, this central block acts as the inertial element whose Coriolis-induced deflections encode the input angular motion. For detection, a photonic crystal optomechanical cavity is integrated between the central and outer mass blocks. Variations in the cavity length modulated by the sensing element's resonant motion can be optically interrogated. Specifically, shifts in the cavity resonance wavelength provide a measurable proxy for angular motion. By segregating driving, sensing, and readout functions into distinct yet interfaced components, this dual-frame gyroscope design aims to leverage the advantages of optical transduction while maintaining essential characteristics such as narrow-band actuation and wide-dynamic range inertial sensing enabled by its mechanical architecture. The following sections will characterize these elements in further detail.

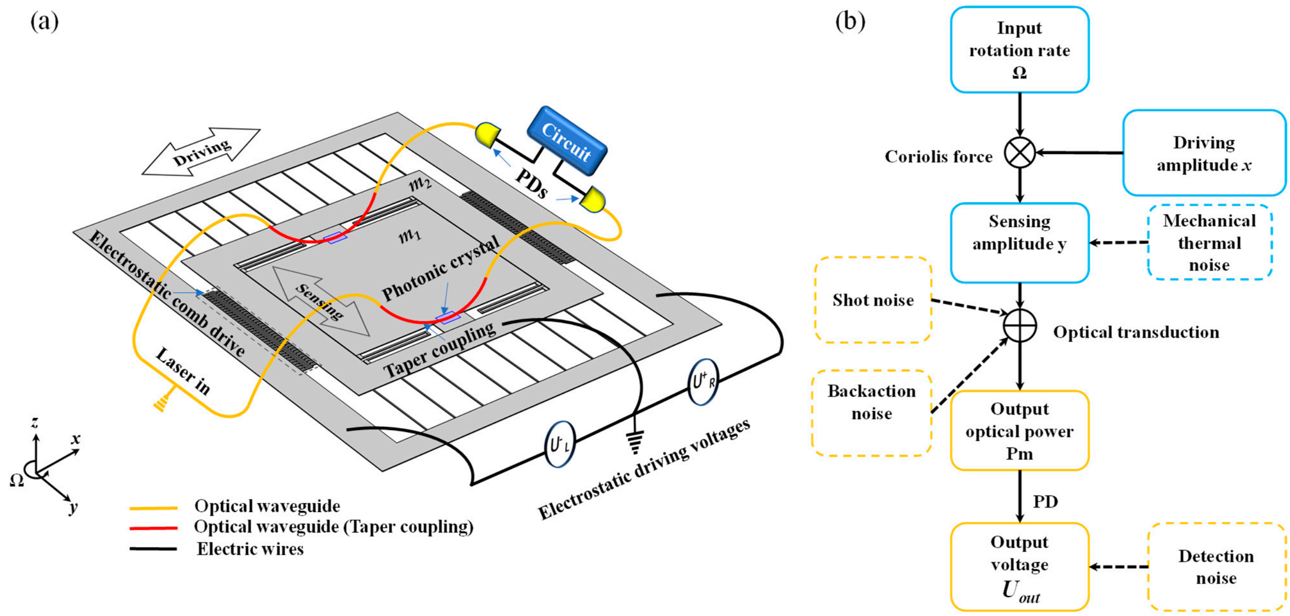

Figure 1. (**a**) A diagram showing the main components of the optomechanical micro-gyroscope, which consists of an electrostatic comb drive, a dual-mass sensing element, and a photonic crystal optomechanical cavity. (**b**) A diagram showing how the optical signal from the cavity is processed by a photodetector and a signal conditioner to measure the angular vibration.

Second, in the angular rate detection configuration, an electrostatic driving force induces simultaneous resonant oscillation of the outer and central masses along the horizontal x-axis. Upon exposure to an external angular vibration about the z-axis, Coriolis forces perturb the central mass perpendicular to its driving mode. Coriolis acceleration is a fictitious force that arises in a rotating reference frame. It is proportional to the angular velocity of the rotation and the velocity of the object in the rotating frame. In our paper, we consider the case of a small angular vibration about the z-axis, which can be modeled as a rotation with a time-varying angular velocity $\Omega_z(t)$. The Coriolis acceleration of a point mass m moving with a velocity v in the rotating frame is given by: $ac = -2\ m\Omega_z(t) \times v$, where $\times$ denotes the cross product. This formula can be derived from the transformation of the acceleration between the inertial and rotating frames. In our paper, we assume that the central mass block of the gyroscope oscillates along the x-axis with a small displacement $x(t)$ and a resonant frequency f_x. The vibration of the central mass block in the rotating frame is then $v = dx/dt = x'(t)$. Therefore, the Coriolis acceleration of the central mass block is: $ac = -2m\Omega_z(t) \times x'(t)$. Since the angular vibration $\Omega_z(t)$ and the displacement $x(t)$ are both harmonic functions of time, we can write them as: $\Omega_z(t) = |\Omega| sin(\omega_\Omega t)$ and $x(t) = A_0\ sin(\omega_x t + \varphi)$, where $|\Omega|$, ω_Ω, A_0, ω_x, and φ are the amplitude, frequency, phase, and initial phase of the angular vibration and the driving motion, respectively. Substituting these expressions into the formula of the Coriolis acceleration, we obtain: $ac = -2m|\Omega|A_0\omega_x\ sin(\omega_\Omega t)cos(\omega_x t + \varphi)$. To simplify the analysis, we assume that the driving frequency ω_x is close to the angular vibration frequency ω_Ω, and the initial phase φ is zero. Then, we can use the trigonometric identity $sin(\alpha)cos(\beta) = 0.5[sin(\alpha + \beta) + sin(\alpha - \beta)]$ to rewrite the Coriolis acceleration as: $ac = -m|\Omega|A_0\omega_x[sin(\omega_\Omega t + \omega_x t) + sin(\omega_\Omega t - \omega_x t)]$. Since we are interested in the response of the central mass block at the angular vibration frequency ω_Ω, we can neglect the term $sin(\omega_\Omega t + \omega_x t)$, which oscillates at a much higher frequency $2\omega_\Omega$. Therefore, the Coriolis acceleration can be approximated as: $ac = -m|\Omega|A_0\omega_x sin(\omega_\Omega t - \omega_x t)$. Finally, by using the small angle approximation $sin(\theta) \approx \theta\ for\ \theta << 1$, we can further simplify the Coriolis acceleration as: $ac = -m|\Omega|A_0\omega_x(\omega_\Omega t - \omega_x t) = -2mf_x|\Omega|A_0(\omega_\Omega t - \omega_x t)$, where we have used the relation $\omega_x = 2\pi f_x$. This is equivalent to the expression of the Coriolis acceleration in our paper: $ac = -2mf_x\Omega_z(t)x'(t)$, where we have replaced $A_0(\omega_\Omega t - \omega_x t)$ by $x'(t)$, the oscillation of the central mass block along the x-axis.

Third, optical interrogation of the dual-mass micro-gyroscope is facilitated using a photonic crystal optomechanical cavity integrated between the central and outer masses. Light from an external laser source is coupled into the cavity via an on-chip waveguide or fiber optic connection. Under the influence of Coriolis-induced vibrations, the central mass oscillates orthogonally to vary the effective cavity length. This modulation manifests as shifts in the cavity's transmission spectrum according to the principles of cavity optomechanics. Specifically, deviations in resonant wavelength Δλ from the cavity's rest state are proportional to changes in gap width Δx induced by Coriolis oscillations of the central mass. Optical power transmitted by the cavity is thereby encoded with information about the input angular vibration. A photodetector then converts the modulated optical transmission into an electrical voltage signal v(t) oscillating at the Coriolis frequency ω_y. Figure 1b shows a block diagram of a signal processing sequence in the MOEMS sensor. Proper characterization of the optomechanical transduction thus enables angular velocity to be resolved from the photodetector voltage with suitable signal conditioning and processing.

For the above designed dual-frame optomechanical gyroscope, the fabrication process of our proposed dual-frame optomechanical gyroscope is based on standard microfabrication techniques, such as lithography, etching, and deposition. The main steps were as follows: we started with a silicon-on-insulator (SOI) wafer with a 250 nm thick device layer and a 2 μm thick buried oxide layer. We used electron beam lithography (EBL) and reactive ion etching (RIE) to define the photonic crystal pattern on the device layer. We used deep reactive ion etching (DRIE) to etch through the device layer and the buried oxide layer to release the mechanical structures, such as the mass blocks and the flexural beams. We deposited a thin layer of gold on the backside of the wafer to form the electrodes for the electrostatic comb drive actuation. We used a dicing saw to cut the wafer into individual chips, each containing a single gyroscope device. The integration of photonic crystal and the MEMS structure was achieved by using a photonic crystal optomechanical cavity as the optical transduction element between the central and outer mass blocks. The photonic crystal cavity was formed by introducing a defect in the periodic array of air holes on the silicon nitride device layer. The cavity supports a localized optical mode that is sensitive to the gap width between the mass blocks. The cavity was coupled to a waveguide or a fiber that delivers the input laser light and collects the output optical signal. The photonic crystal cavity and the MEMS structure were fabricated on the same device layer, which ensures the alignment and robustness of the integration.

2.2. Theoretical Description of Optomechanical Coupling

Optomechanical cavities are commonly interfaced using tapered optical waveguides or fibers to facilitate light coupling and output, as shown in Figure 2a. The fundamental cavity-waveguide interaction dynamics are governed by input–output relations derived from classical cavity optomechanics theory [26,27]. Specifically, the intra-cavity optical field amplitude 'a' experiences external coupling to the waveguide or fiber at a rate κ_e, as well as intrinsic dissipation to the surrounding environment at a rate κ_i. These rates characterize the photon escape channels from the optical resonance and determine the cavity linewidth. In accordance with the well-established input-output framework and using the classical optical cavity coupling theory [28,29], the steady-state response of the intracavity field amplitude, denoted by the operator 'a', to an input field with amplitude 'a_{in}' is described by the following relation:

$$\frac{da}{dt} = -i\Delta a - \frac{\kappa}{2}a + \sqrt{\kappa_e}a_{in} \quad (1)$$

where $\Delta = \omega_l - \omega_c$ represents the laser detuning rate of the laser resonant frequency ω_l and the optical cavity resonant frequency ω_c, $|a_{in}|^2 = P_{in}/\hbar\omega_l$, P_{in} is the input laser power, and $\hbar$ is the Planck constant. The total coupling rate κ is the sum of the external coupling rate and internal coupling rate, $\kappa = \kappa_e + \kappa_i$, and the optical quality factor is $Q_{opt} = \omega_c/\kappa$. The maximum value of this derivative occurs when k_e/k is 0.5, which corresponds to the critical coupling condition where all the light coupled into the cavity is dissipated into the environment.

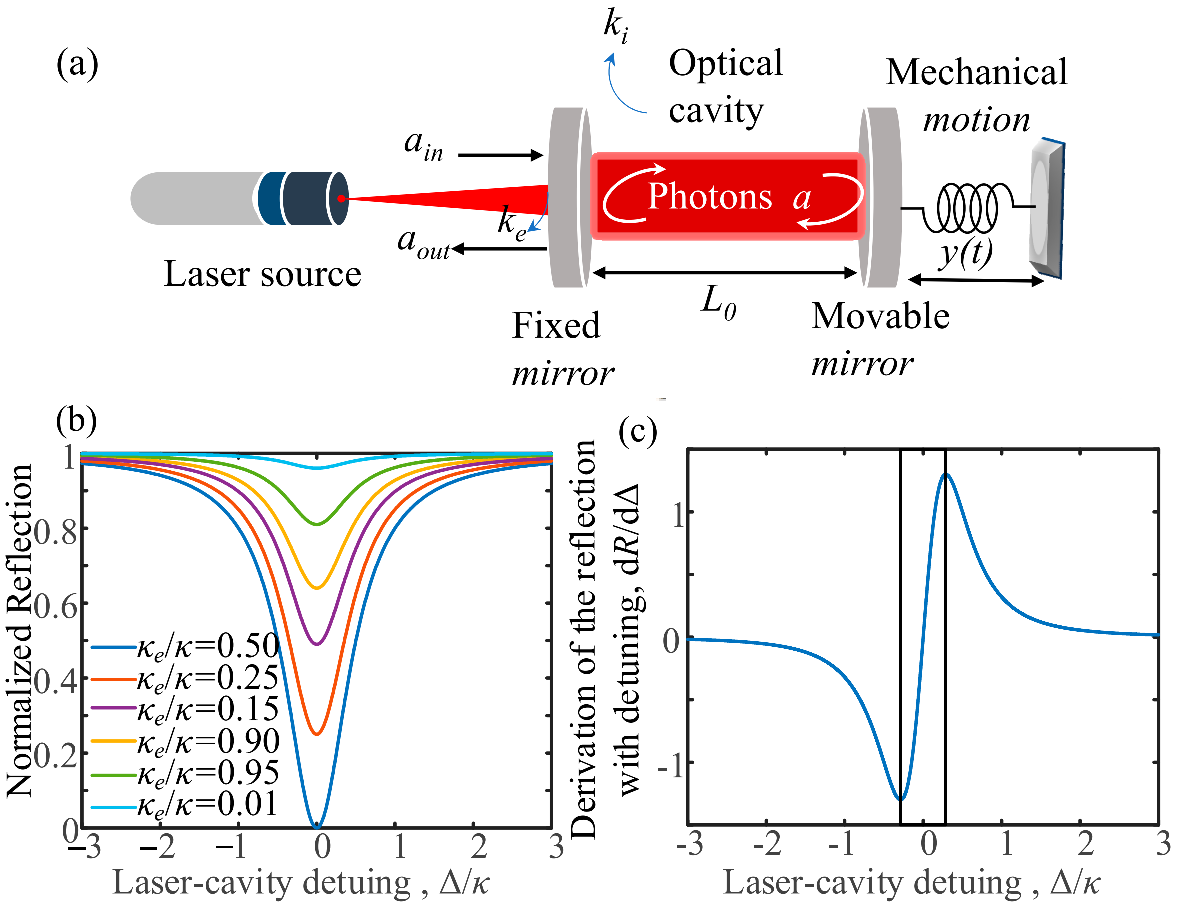

Figure 2. Optical characteristics of the optomechanical cavity. (**a**) a single-sided coupling scheme, illustrates an optomechanical system with a laser source, and an optical cavity with a movable mirror. (**b**) show reflectance variation with detuning rate. Note how the reflection on resonance approaches zero as κ_e/κ approaches 1/2. This is because when $\kappa_e = \kappa/2$, then $\kappa_e = \kappa_i$, and all light is lost to the surrounding environment, and when κ_e/κ approaches 1, the reflection on-resonance approaches unity. This is because as κ_e approaches κ, essentially no light is lost to the surrounding environment via κ_i, (**c**) The phase of the reflected light field as a function of detuning for the ratio of κe/κ = 0.5.

This work elucidates the fundamental coupling between the guided optical modes of the waveguide/fiber and intrinsic cavity electromagnetic modes, forming the theoretical basis for optomechanical transduction in the gyroscopic system. A rigorous quantitative characterization of the external (κ_e) and intrinsic (κ_i) decay rates from the optical cavity and their impact on transmission and reflection dynamics imperative for optimizing the interfacing optics and readout methodology. The following sections aim to simulate these cavity parameters and modal dynamics numerically via time–domain solutions. Based on the steady-state condition with the time derivative of the intracavity field amplitude ($\mathrm{d}a\,/\mathrm{d}t = 0$), and derived from Equation (1) upon applying this steady-state assumption such that the intracavity field 'a' reaches a constant value over time balancing the drive and dissipative terms, Equation (1) can be rearranged as follows to solve for the steady-state field amplitude 'a' [28–32]:

$$a = \sqrt{\kappa_e} a_{in} / (i\Delta + \frac{\kappa}{2}) \tag{2}$$

Furthermore, the amplitude of the output field is described by a relation involving the input field amplitude and the intracavity field amplitude, as established by the pertinent cavity input–output theory [18,33–36], we obtain:

$$a_{out} = -a_{in} + \sqrt{\kappa_e} a \tag{3}$$

By substituting Equation (2) into Equation (3) and using algebraic manipulations. The expression for R will have terms applying k_e, k_i, and Δ, and by simplifying, we can rearrange the terms to obtain the normalized optical reflection $R \equiv |a_{out}/a_{in}|^2$, transmitted through the waveguide when we couple a laser to such an optical cavity and waveguide system.

$$R = |a_{out}/a_{in}|^2 = 1 - \frac{k_e k_i}{\Delta^2 + k^2/4} \tag{4}$$

According to Equation (4), the reflection spectrum presents a negative Lorentzian function in terms of laser-cavity detuning (seen in Figure 2b). We can see that the relationship between R and Δ can be divided into under-coupling ($\kappa_e < \kappa/2$), critical-coupling ($\kappa_e = \kappa/2$), and over-coupling ($\kappa_e > \kappa/2$). Specifically, in under-coupling, R decreases from 1 to 0 with the increase in κ_e/κ from 0 to 1/2. With the rise in κ_e/κ from 1/2 to 1, the Lorentzian dip of R gradually disappears, and R returns to 1. In more exceptional cases, when κ_e/κ is much less than 1, almost no light is coupled into the optical cavity ($R \approx 1$). And when κ_e/κ is close to 1, all the light coupled into the optical cavity is almost not dissipated, and all the light is coupled back to the waveguide ($R \approx 1$). However, in the critical coupling, all the light coupled into the optical cavity is dissipated into the environment, and the R is 0. Moreover, the amplitude variation relation of $\mathrm{d}R/\mathrm{d}\Delta$ is further studied, and the maximum value of $\mathrm{d}R/\mathrm{d}\Delta$ is directly shown in Figure 2c, which will be further discussed in Section 2.3. It should be noted that due to the small and unstable R of the shaded area in Figure 2c (visually shown in Figure 2b), the locking cavity-laser detuning rate Δ should be kept away from the shaded area in practice. We reported the uncertainty or error estimates for our simulation results by calculating the standard deviation and confidence interval for each performance metric, such as the scale factor, angle random walk, and optomechanical coupling rate.

2.3. Optomechanical Sensing of Displacement and Angular Vibration

The proposed dual-frame optomechanical gyroscope possesses an orthogonalized structural configuration as illustrated in Figure 3a. Under idealized operating conditions, the decoupled design behaves as two independent single degree-of-freedom spring-mass-damping systems along orthogonal x- and y-axes. When functioning as an angular rate sensor, the gyroscope drives the outer mass resonantly along the drive axis (x-direction) while the Coriolis force perturbs the central mass along the orthogonal detection axis (y-direction), as previously described. If the resulting vibrational displacements are assumed small enough to satisfy the linearization approximation, yet the driving motion remains much larger than the Coriolis response, the gyroscope dynamics can be expressed as two linearly coupled simple harmonic oscillators [37–39]:

$$\begin{cases} \ddot{x} + 2\xi\omega_x\dot{x} + \omega_x^2 x = F_{drive}/m_x \\ \ddot{y} + 2\xi\omega_y\dot{y} + \omega_y^2 y = F_{Coriolis}/m_y \end{cases} \tag{5}$$

where x and y are the displacements in driving and sensing directions, respectively; ξ parametrizes damping, ω_x and ω_y are the angular resonant frequencies, m_x and m_y are the equivalent mass of the driving mode and detection mode; and the drive/Coriolis forces are treated as perturbations. Numerical simulation of these governing equations of motion will enable the characterization of key performance metrics in subsequent sections. The Coriolis force $F_{Coriolis} = -2m_y\Omega\dot{x}$, the gyroscope dynamics equations can be better described by:

$$\begin{cases} m_x\ddot{x} + c_x\dot{x} + k_x x = F_{drive} \\ m_y\ddot{y} + c_y\dot{y} + k_y y = -2m_y\Omega\dot{x} \end{cases} \tag{6}$$

where k_x, c_x, k_y and c_y are the coupled oscillator equations of motion containing stiffness and damping coefficients corresponding to the orthogonal driving and detection vibration modes. From linear systems theory, these spring and damping parameters are related to the effective mass m and angular resonant frequencies ω_x and ω_y through: $k_x = \omega_x{}^2 m_x$, $c_x = 2\xi\omega_x m_x$, $ky = \omega_y{}^2 m_y$, $c_y = 2\xi\omega_y m_y$. Here, dot notation signifies a derivative concerning time. This establishes the analytical basis for characterizing the gyroscope dynamics using physical system parameters like resonance frequencies, damping, and time-varying input angular rate excitation. The numerical solution of the governing equations will enable performance evaluation under varying conditions.

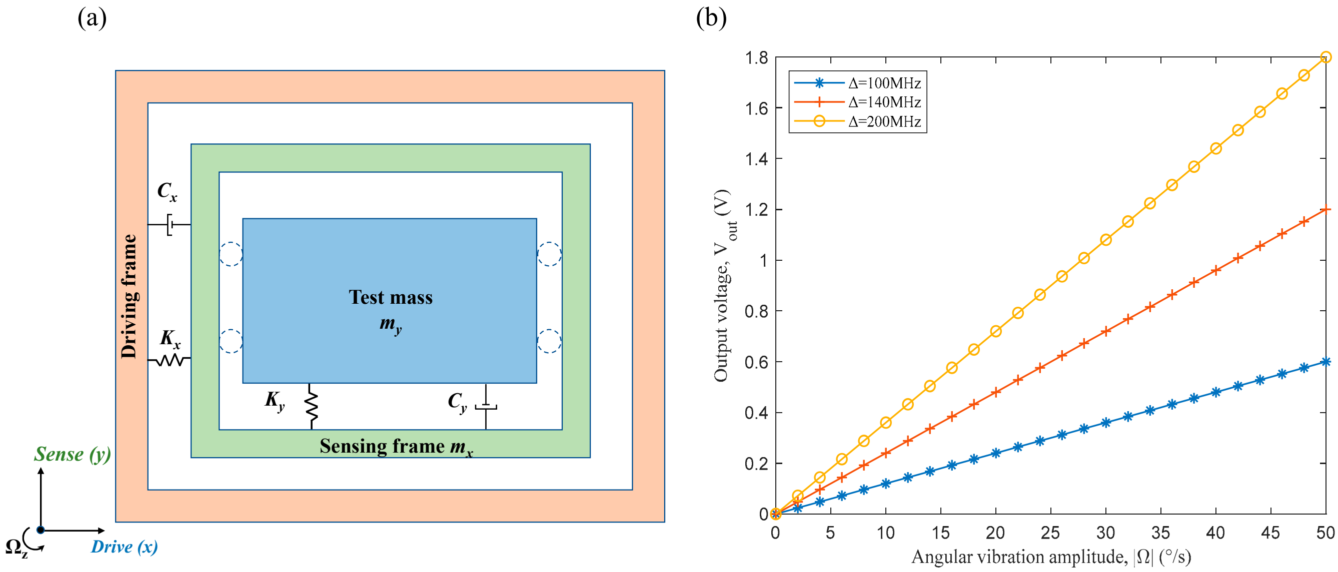

Figure 3. (**a**) Schematic representation of the dual-frame optomechanical gyroscope under zero angular velocity; (**b**) simulated relationship between the output voltage of the gyroscope and the input angular vibration.

Based on Equation (6), the displacement of the sensing mode is regarded as a harmonic motion under the stable condition. Because the test range is limited, we just chose the low frequency of $y(t)$ to measure the amplitude and frequency of angular vibration, $y_{low}(t) = 0.5A\cos{(\omega_\Omega - \omega_x)}$.

As illustrated in (Figure 2a), the optical resonance frequency of the photonic crystal cavity is coupled to the mechanical vibrational motion of the dual-frame structure via the optomechanical interaction. In the linear response regime of small displacements, perturbation theory establishes that variations in cavity length $y(t)$ induce a shift in resonance frequency $\omega_c{}'$ that is linearly proportional to the displacement [28]. This relationship can be expressed as: $\omega_c{}' = \omega_c + g_{om}y(t)$, ω_c is the unperturbed cavity frequency at $y(t) = 0$, and the optomechanical coupling rate $g_{om} = \partial\omega_c{}'/\partial y$ quantifies the transduction efficiency between mechanical and optical domains. By setting a fixed detuning between the laser drive frequency and ω_c, shifts in $\omega_c{}'$ due to vibrations along either orthogonal mechanical mode will manifest as changes in cavity transmission/reflection. A photodetector linked to the output waveguide can therefore resolve the amplitude and phase of both motional components by monitoring interference of the modulated optical signal. This dual-axis transduction scheme underlies the ability to isolate Coriolis-induced signals corresponding to input angular vibrations, as discussed previously. Numerical simulation of these cavity dynamics will provide further insight into optomechanical performance.

The transmitted optical power P_m after interacting with the optomechanical system can be modeled based on the standard input–output relations of cavity optomechanics theory [40]. Specifically, for a laser driven at angular frequency ω_l that is coupled to an optical cavity of frequency ω_c with optomechanical coupling rate g_{om} and dissipation rates κ and γ_m, the steady-state mean cavity photon number $<n> = (k/2)^2 / |(k/2) - i(\Delta - g_{om}y)|^2$ and output power P_m are given by:

$$P_m = P_{in}\eta \frac{dR}{dy} g_{om} y(t) = P_{in}\eta \frac{dR}{d\Delta}\frac{d\Delta}{dy} y(t) = P_{in}\eta \frac{dR}{d\Delta} g_{om} y(t) \tag{7}$$

where η represents some realistic losses from the cavity to the detector. Through the change in light power, the displacement of the gyroscope detection mode is detected, and the amplitude of angular vibration is calculated. The final total output voltage is shown in Figure 3b. The larger the angular vibration, the larger the voltage output, which is discussed in Section 3.3. Numerically simulating Equation (7) would enable the characterization of how the output optical power P_m is modulated by the vibrational dynamics induced in the optomechanical cavity. This provides the theoretical framework for modeling optical transduction and readout in the gyroscope system.

3. Driving and Sensing Performance Analysis

3.1. Design and Analysis of Driving a Mechanical Sensitive Structure

Various actuation mechanisms have been implemented for resonantly driving the inertial masses in MEMS gyroscopes. Electrostatic comb drives represent a widely adopted solution due to advantages such as facile fabrication using standard microfabrication techniques, low power operation, and capacity for sufficient displacements. As illustrated in Figure 4a, a comb drive comprises interleaved fixed and movable sets of parallel electrodes (teeth). When an electrical potential is applied between the combs, electrostatic forces induce an oscillating transverse motion along the x-axis. The geometry is characterized by the overlap length l_f of opposing tooth surfaces, the width b_f of each tooth, and the gap distance a_f separating adjacent teeth.

The analytical model of comb drive actuation is well established [39,41]. Based on parallel plate capacitor theory, the resulting electrostatic force F_{drive} between a single tooth-pair is given by:

$$F_{drive} = \frac{4n\varepsilon_0 h U_d U_a cos(\omega_d t)}{d} \tag{8}$$

where n is the number of comb teeth, h is the thickness, d is the parallel spacing between comb teeth, ε_0 is the vacuum dielectric constant. U_d is the DC voltage set as 5 V and the frequency of the driving force depends on the input AC electrical signal, $U_a cos\omega_d t$ with U_a is 10 V.

A major consideration in the design of dual-mass optomechanical gyroscopes is decoupling the orthogonal driving and sensing vibrational modes to minimize cross-axis interference. The Coriolis force enables the rate output of a gyroscope by transferring drive motion into a detectable sense motion proportional to the input rate.

This work presents a support structure employing U-shaped and folded flexure beams aimed at reducing equivalent stiffness and inter-modal coupling, as shown in Figure 4b. Flexural beams are widely used in MEMS designs due to their ability to facilitate motion along defined axes while providing structural support. Prior work has shown that the stiffness of a U-shaped flexure beam K_{Ux} can be approximated as two straight beams connected in series for motion along the axis.

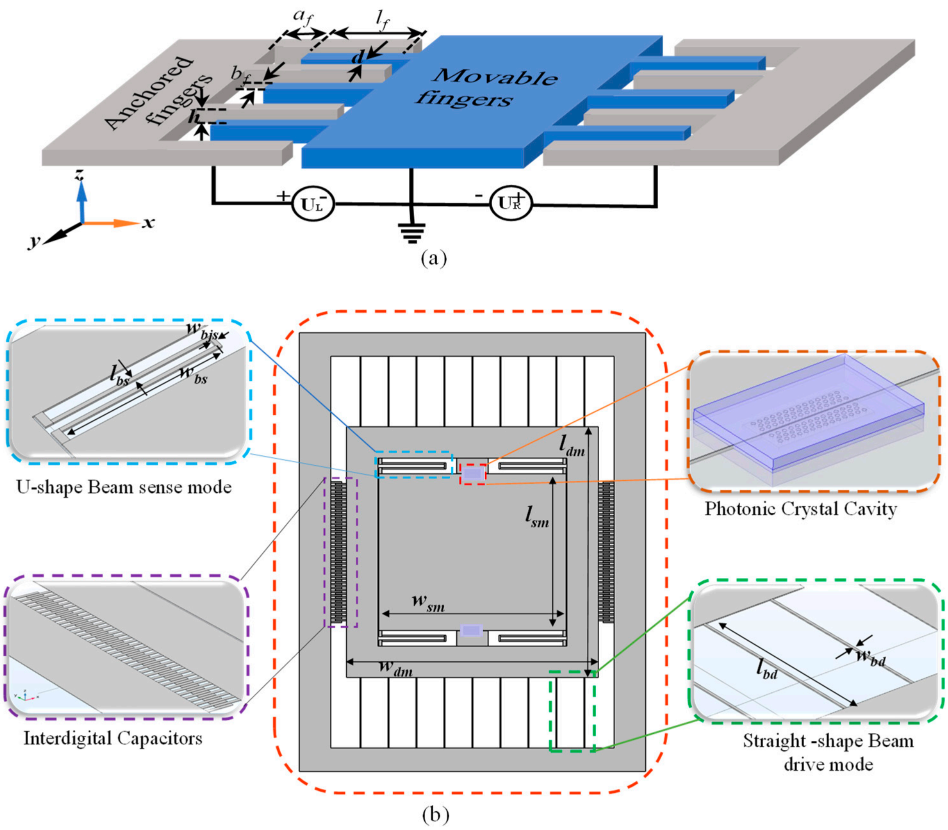

Figure 4. (**a**) Pull-off electrostatic comb driving structure diagram; (**b**) the structural design of the optomechanical micro-gyroscope.

Specifically, the equivalent stiffness of the U-shaped beam in the sensing y-direction is given by:

$$K_{Ux} = \left(\frac{EI}{l_1} + \frac{EI}{l_2}\right) - 1 = E\frac{W_{bs}^3 h}{2l_{bs}^3} \tag{9}$$

where K_x represents the stiffness coefficient; E is the Young's modulus, I is the cross-sectional moment of inertia, and l_1 = l_2 = l_{bs} are the lengths of the individual U-shaped segments, respectively. w_{bd}, l_{bd} are the width and length of the straight beam, respectively. It can be seen from Equation (9) that the stiffness coefficient of a U-shaped beam is half that of a straight beam. Moreover, the structure can eliminate the residual stress generated by nano-machining and restrain the resonance frequency change brought by the residual stress. The analytical approach provides the theoretical grounding for evaluating the proposed support architecture's effectiveness in decoupling modal responses.

Based on the analytical modeling presented, finite element analysis (FEA) was conducted to numerically simulate and optimize key design parameters of the gyroscope. Table 1 summarizes the optimized structural configuration obtained through this process. Generally, lower resonant frequencies benefit mechanical sensitivity but also susceptibility to external perturbations. Therefore, the driving and sensing modes were optimized to have angular frequencies of 61,969 Hz and 61,811 Hz, respectively, for effective operation. Additionally, a thickness of ~250 nm was chosen for the structural layers to realize the desired optical properties of the photonic crystal optomechanical cavity.

Table 1. Structural parameters of cavity optomechanical high precision micro-gyroscope.

Symbol	Quantity	Value
$l_{Gyro} \times w_{Gyro}$	Gyro dimension	280 μm × 220 μm
h	Thickness of gyroscope	0.25 μm
l_{comb}	Comb-tooth capacitor length	1 μm
w_{comb}	Comb-tooth capacitor width	7 μm
l_{bd}	Driving beam length	45 μm
w_{bd}	Driving beam width	0.65 μm
l_{bs}	Sensing U-beam length	1 μm
w_{bs}	Sensing U-beam width	39.667 μm
l_{bjs}	Sensing U-beam join length	4 μm
w_{bjs}	Sensing U-beam join width	1 μm
d	Gap between comb teeth	500 nm
n	Number of comb teeth	40
l_{dm}	Drive mass length	160 μm
w_{dm}	Drive mass width	160 μm
w_{sm}	Sense mass width	119 μm
l_{sm}	Sense mass length	100 μm
Q	Mechanical Q-factor	10,000

The gravitational deflection of the dual masses is calculated by applying a static load of mg to each mass, where m is the effective mass and g is the gravitational acceleration. The deflection along the z-axis is obtained by solving the equation of equilibrium for each mass:

$$\sum F_z = k_z \Delta z - \ mg = 0 \tag{10}$$

where k_z is the equivalent stiffness coefficient along the z-axis, and Δz is the displacement. The stiffness coefficient k_z is derived from the geometry and material properties of the flexural beams, as follows:

$$k_z = \frac{Ebh^3}{4l^3}\left(\frac{3}{2} + \frac{1}{2}cos\frac{\pi l}{2a}\right) \tag{11}$$

where $b = w_{bd}$ and h = 250 nm are the width and thickness of the beam, $l = l_{bd}$ is the length of the beam, and $a_d = l_{bd}$ is the distance between the fixed and movable ends of the beam.

The simulation of z-axis displacement under gravity is performed using finite element analysis (FEA) software COMSOL Multiphysics (version 6.1). The model consists of a silicon substrate and two silicon nitride masses connected by flexural beams. The material properties and dimensions are taken from Table 1. A fixed boundary condition is applied to the substrate, and a gravity load of 9.81 m/s^2 is applied to the masses. The displacement field along the z-axis is computed by solving the linear elasticity equations for the model. The maximum relative displacement between external and sensing masses was found to be 3.48 nm, which is negligible compared to the gap width of 100 nm. Therefore, gravity has minimal impact on the optical characteristics or optomechanical transduction of the gyroscope, as shown in Figure 5a,b.

Based on the finite element analysis, the simulated gyroscope design allows further evaluation of the driving performance and detection capabilities. Figure 6a demonstrates that increasing the number of comb electrodes and applied voltage augments the electrostatic driving force and resulting displacements, as expected, based on parallel plate capacitor theory.

Figure 6b plots driving displacement versus excitation frequency, showing resonant behavior near 61,969 Hz as per the optimized driving mode parameters. Peak displacement approaches 1.75 μm, sufficient for the intended operation. Equation (5) governs how Coriolis acceleration induced by external angular vibration is transduced to a sensed displacement. As seen in Figure 6c, this transduction efficiency decreases with a widening frequency split between driving and sensing resonances. However, packaging the device under vacuum conditions is expected to raise intrinsic Q factors, mitigating impacts from a non-zero split. Overall, the simulated design metrics indicate the gyroscope concept could realize angular velocity detection within target specifications once fabricated and experimentally validated. Continued modeling would provide additional design insight.

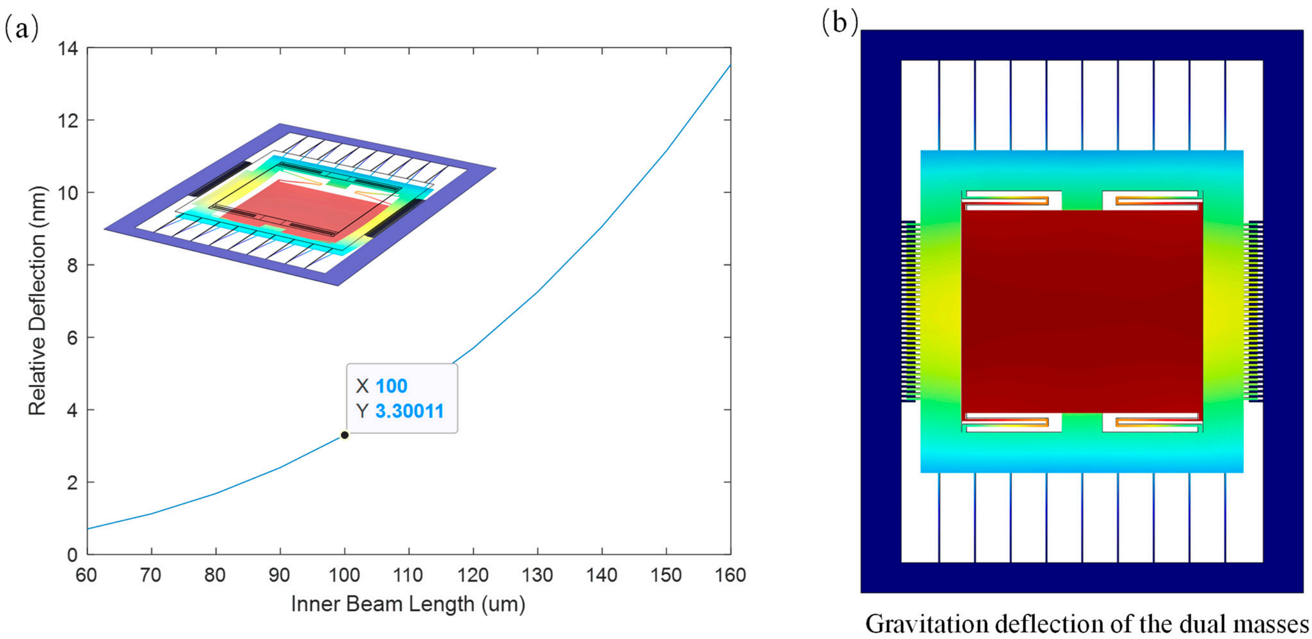

Figure 5. (**a**) Calculating and simulating the gravitational deflection of the dual masses in an optomechanical gyroscope, (**b**) the simulation of z-axis displacement under gravity. The maximum relative displacement between external and sensing masses under gravity load was constrained to less than 3.5 nm at real length of inner beam.

3.2. Simulation of Photonic Crystal Cavity Characteristics of Optomechanical Gyroscope

Based on the photonic crystal theory, we simulated the typical photonic crystal cavity performances by COMSOL and FDTD. Table 2 presents the optimized structural configuration derived from this procedure in a summarized form. with the refractive index of silicon nitride is 2.0 and the refractive index of air is 1.0 at the operating wavelength of 1.564 µm. The optical resonance frequency of the fundamental optical mode concerned in this paper is 200.69 THz, and the optical quality factor is 2.6×10^5.

Table 2. Structural parameters of photonic crystal.

Quantity	Value
Length of crystal	7 µm
Width of crystal	3.3 µm
Period of topology	470 nm
Air gap	100 nm
Distance between hole and air gap	438 nm
Distance between hole and center of structure	235 nm
Thickness of crystal	250 nm
Radius of hole	134 nm
Displacement of hole	5/10/15 nm

When the gyroscope is in working mode, the applied angular vibration will cause the gap width of the photonic crystal cavity to be changed. Therefore, it was found that the change in gap widths of the photonic crystal cavity would lead to a dispersion effect (optical system of the optomechanical micro-gyroscope, and signal-processing sequence in an optical-sensing system shown in the illustration in Figure 1). The simulated photonic crystal resonance wavelength with different gap widths is shown in Figure 6d.

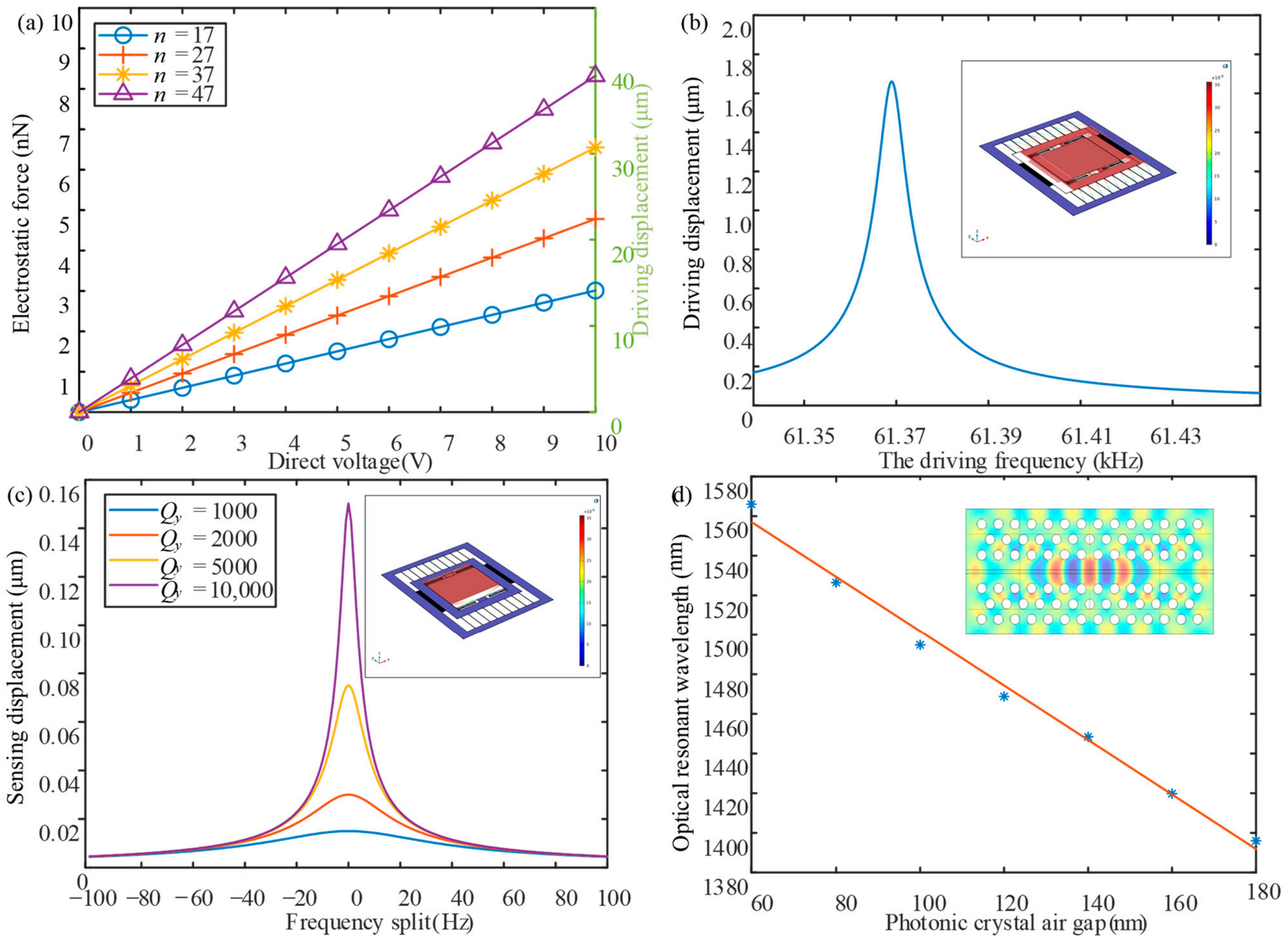

Figure 6. (**a**) Measured variation in the driving electrostatic force for different DC voltages under different numbers of comb electrodes, (**b**) change in displacement amplitude of the driving mass for driving frequency; the inset figure shows the frequency of the driving mode, indicating a resonant frequency of 61,969 Hz, (**c**) variation in sensing mass displacement amplitude for frequency split with increasing mechanical quality factor; the inset figure shows the frequency of the sensing mode, indicating a resonant frequency of 61,811 Hz, (**d**) shows measurement of the variation in optical resonance wavelength with the width of the photonic crystal air gap; the inset figure shows the photonic crystal optomechanical cavity structure and its transmission spectrum.

3.3. Performance Analysis of Micro-Gyroscope Based on Optomechanical System

The primary performances discussed in the paper for the micro-gyroscope are scale factor (sensitivity) and angular random walk (noise limit). In general, a large-scale factor helps to improve the signal-to-noise ratio (SNR) and bias stability and increases the Coriolis coupling from the driving mode to the sensing mode. Furthermore, the noise limit consists of four parts: mechanical thermal noise [32], detection noise, shot noise, and back-action noise. In the paper, the scale factor of the optomechanical gyroscope is the linear correlation between the output voltage V_{out} and the amplitude of the angular vibration $|\Omega|$. The total scale factor SF is composed of the mechanical sensitivity (S_m), the optomechanical sensitivity (S_P) of the cavity optomechanical system, and the voltage sensitivity (S_V) of the photodetector, which is expressed as:

$$SF = \frac{V_{out}}{|\Omega|} = S_{mech} \cdot S_P \cdot S_V \tag{12}$$

The mechanical sensitivity S_m is defined as the ratio of the displacement amplitude of the sensing mode to $|\Omega|$.

$$S_m = \left|\frac{0.5A}{\Omega}\right| = \frac{F_{drive}Q_x}{m_x\omega_0\sqrt{(\omega_y{}^2-\omega_0{}^2)+\omega_y{}^2\omega_0{}^2/Q_y{}^2}} \tag{13}$$

We have detailed the relationship between output power P_m and displacement of sensing mode in Section 2.3. Therefore, based on Equation (7), SP is expressed as:

$$S_p = \frac{P_m}{y} = P_{in}\frac{dR}{dy}\eta = P_{in}\eta\frac{dR}{d\Delta}g_{om} \tag{14}$$

In this paper, the PIN-TIA photodetector is selected, where S_V = 65 V/W. The random white noise in the system results in a zero-mean angle error, which is described by *ARW*. The ARW_{total} can characterize the short-term performance of the optomechanical gyroscope [32], which is:

$$ARW_{total} = \sqrt{ARW_{mech}{}^2 + ARW_{NEP}{}^2 + ARW_{SN}{}^2 + ARW_{ba}{}^2} \tag{15}$$

By substituting the equivalent thermal noise power spectral density of the proven mass into the mechanical motion Equation (5), the ARW_{mech} is:

$$ARW_{mech} = \sqrt{\frac{4k_BTe\omega_mQ_y}{m_y(Q_y{}^2(-2\omega_m\omega_\Omega+\omega_\Omega{}^2)^2+(\omega_m{}^2-\omega_\Omega\omega_m)^2)}}\cdot\frac{1}{S_m} \tag{16}$$

where k_B is the Boltzmann constant, and *Te* is the temperature. The electronic noise of photodetectors is usually measured by noise equivalent optical power (*NEP*). Therefore, the equivalent ARW_{NEP} of an optomechanical gyroscope can be obtained by converting the equivalent noise at the output of the detector through scaling factors:

$$ARW_{NEP} = \frac{NEP}{P_{in}\eta\left|\frac{dR}{d\Delta}g_{om}\right|\cdot S_m} \tag{17}$$

Meanwhile, there is also shot noise in the laser-light field obeying Poisson statistics, which can be converted to equivalent *ARW*:

$$ARW_{SN} = \frac{\sqrt{2\hbar\omega_\ell P_{\det}\eta_{qe}}}{P_{in}\eta\left|\frac{dR}{d\Delta}g_{om}\right|\cdot S_m} \tag{18}$$

where P_{det} and η_{qe} are the optical power and quantum efficiency of the detector, respectively. Furthermore, in the optomechanical system, the shot noise exerts the reaction force and causes the photonic crystal to move, which is the back-action noise:

$$ARW_{ba} = \frac{2\hbar g_{om}Q_y}{m_yS_m}\sqrt{\frac{2n_c}{\kappa(Q_y{}^2(-2\omega_m\omega_\Omega+\omega_\Omega{}^2)^2+(\omega_m{}^2-\omega_\Omega\omega_m)^2)}} \tag{19}$$

Based on the above theoretical analysis, the influence of input power and laser-cavity detuning on the gyroscope proposed in this paper is discussed in detail. Specifically, those parameters $\Delta = -\kappa/2$, $\kappa_e = 1.5 \times 10^8$, $\kappa_i = 0.5 \times 10^8$ and g_{om} = 3 GHz/nm are chosen in this paper for a joint optomechanical cavity. Because the optomechanical sensitivity changes linearly with the input laser power, the total sensitivity increases with the increase in the light power, and at the same time, the noise caused by the detector and shot noise decreases with the rise in the power (as seen in Figure 7a,b). Meanwhile, the number of photons in the cavity increases rapidly, resulting in the increased optomechanical coupling and a rise in the back-action noise. However, the shot noise, detection noise and back-action noise usually are smaller than mechanical thermal noise. The sensitivity can be significantly improved by choosing appropriate laser-cavity detuning, as shown in Figure 7c. When $\Delta = -\kappa/2$, the scale factor is 22.8 mV/(°/s) [30]. As shown in Figure 7d, although all other noises except thermal noise are affected by laser-cavity detuning, ARW_{total} is mainly affected by mechanical thermal noise. Moreover, the mechanical thermal noise has a Lorentzian function as the frequency. When the detection frequency deviates from the mechanical resonance frequency, the thermal noise will decrease rapidly due to the angular vibration frequency (as seen in Figure 8). However, the low-frequency noise of the detector is considerable, which limits the bandwidth of angular vibration.

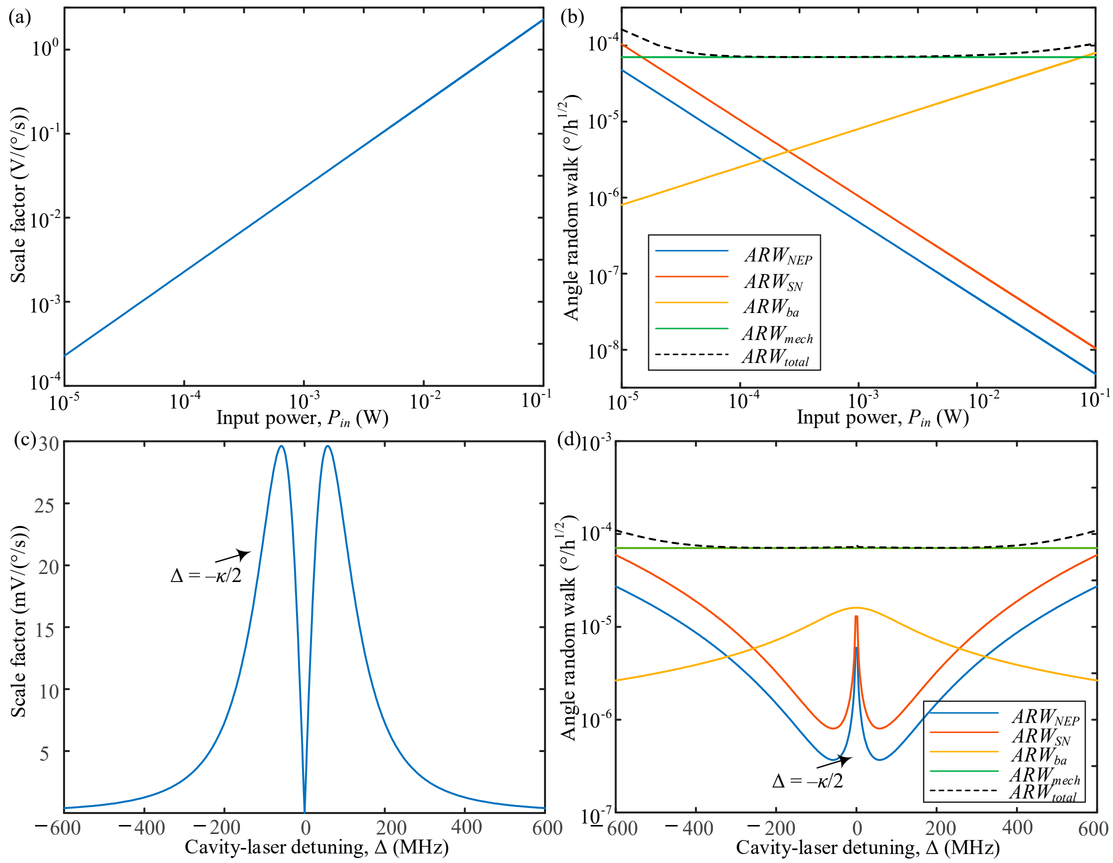

Figure 7. (**a**) Performance analysis of an optomechanical dual-mass gyroscope under varying laser input conditions based on the standard parameters of a silica resonator. (**a**) scale factor, drive amplitude, and (**b**) the laser input power governing ARW. Cavity-laser changes (**c**) the normalized SF, SM, and SP, and (**d**) the magnitude of the ARW detuning Δ.

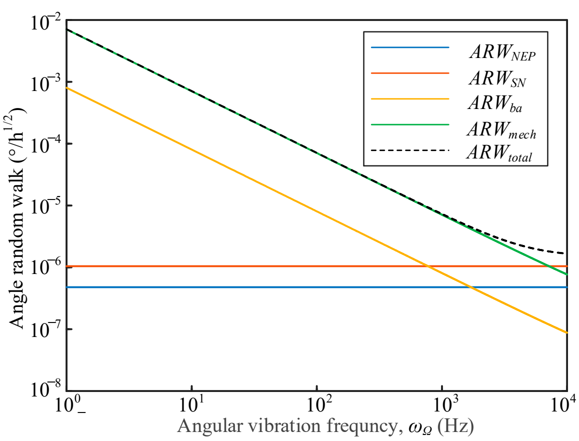

Figure 8. Angular Random Walk variation as a function of angular vibration frequency.

4. Comparative Study

In this section, we compare the performance characteristics of previously reported high-precision micro-opto-electro-mechanical systems (MOEMS) gyroscopes to our novel dual-frame optomechanical gyroscope architecture incorporating an integrated photonic crystal cavity. As summarized in Table 3, three earlier frame-type MEMS gyroscope designs utilized an electrostatic comb drive actuator and displacement sensor [39,42,43]. However, these approaches exhibited limitations associated with electronic noise introduced by the driving and sensing methods employing different operating modes. Additional MOEMS gyroscopes employing an electrostatic comb drive and optical output for sensing displacement were impacted by sensitivity to environmental fluctuations and the need for a high optical quality photonic crystal fabrication [12]. For effective operation to counter challenges in achieving perfect coaxial alignment of optical and mechanical axes in practice [23]. Suffered limited resolution and bandwidth from a low mechanical quality factor [24]. Increased complexity, susceptibility to lock-in effects, vibrational noise sensitivity, calibration requirements, constrained detectable angular velocity ranges, assumptions of low rotation rates, and dependence on quadrature phase detection [25]. In contrast, our novel dual-frame optomechanical gyroscope architecture, as theoretically analyzed, has demonstrated superior performance characteristics including the highest simulated sensitivity and lowest noise levels at an input laser power of 3mW. Additionally, this design offers advantages such as low cost, and extremely miniaturized dimensions for an ultralight test mass. Importantly, the optical detection method is unaffected by electromagnetic interference and incorporates negligible thermal electronic noise, exhibiting a high signal-to-noise ratio approaching only unavoidable quantum noise levels. Therefore, our novel gyroscope architecture represents a promising solution for next-generation inertial measurement applications.

Table 3. Comparative evaluation of sensing performance metrics for micro-optomechanical systems (MOMES) and MEMS gyroscope with novel dual-frame optomechanical gyroscope designs based on theoretical/numerical simulations.

Gyroscope Type	Structure	Proof Mass	Resonator Size	Driving Method	Sensitivity	ARW (°/h$^{1/2}$)
(Multi-DoF) MEMS gyroscope [42]	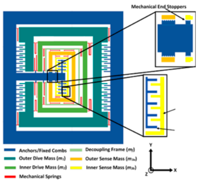	≈1.103 µg	4.2 × 4.2 mm × mm	Electrostatic comb electrodes	198.9 V/(○/s),	-
Dual-mass resonant MEMS gyroscope [39]	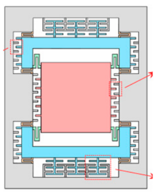	≈10.7 µg	1557 × 1816 µm × µm	Electrostatic comb electrodes	4.6433 × 10^{-4} µm/(○/s)	-
Single-drive multi-axis MEMS gyroscope [43]	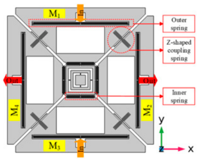	≈0.279 mg	300 × 300 mm × µm	Electrostatic comb electrodes	Cross-axis sensitivities for x and y-axis 0.482% and 0.120%,	-
MOEMS [12]	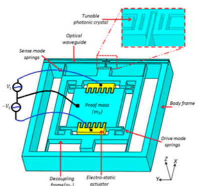	15 µg	405 µm^2	Electrostatic comb electrodes	0.051 nm/(○/s)	-

Table 3. *Cont.*

Gyroscope Type	Structure	Proof Mass	Resonator Size	Driving Method	Sensitivity	ARW (°/h$^{1/2}$)
Gyroscope with two-dimensional optomechanical mirror [23]	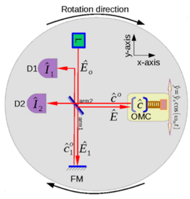	1.83 mg	Dimensional mirror with a diameter 1 mm and a thickness of 0.5 mm	Optomechanical	10^{-11} rad/s/Hz$^{1/2}$	
Optomechanical gyroscope [24]	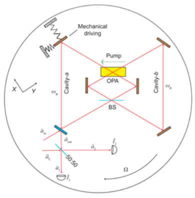	4.77 mg	Dimensional mirror with a diameter 1.5 mm and a thickness of 0.5 mm	Optomechanical	10^{-5} rad/s/Hz$^{1/2}$	
Optomechanical gyroscope [25]	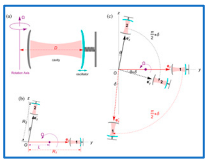	2.62 mg	Dimensional mirror with a diameter 1.2 mm and a thickness of 0.5 mm	Optomechanical	10^{-9} rad/s/Hz$^{1/2}$	-
MOEMS	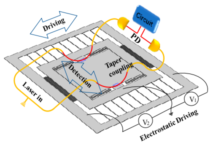	14 ng	280 × 220 µm	Electrostatic comb electrodes	22.8 mV/(○/s)	7.1×10^{-5} (°/h$^{1/2}$)

5. Conclusions

In this paper, we proposed a novel and significant dual-frame optomechanical gyroscope design, which integrates optical cavity interactions with mechanical resonant motion to achieve high angular resolution and sensitivity. We explained how our design overcomes the limitations and challenges of traditional MEMS gyroscopes that rely on electronic transduction and readout, such as noise, and stability issues. Such an optomechanical gyroscope comprises a pull-off electrostatic comb drive structure, test mass, and photonic crystal sensing structure. The operation principle of the new gyroscope including the Coriolis force transduction based on the optomechanical coupling was analyzed and discussed to prove that the angular vibration can be measured precisely. Moreover, the parameter selection and optimization of the sensitive structure and photonic crystal optomechanical cavity were studied utilizing finite element simulation. Under the appropriate electrostatic force, the optomechanical gyroscope can achieve SF = 22.8 mV/(°/s) and ARW = 7.1×10^{-5}(°/h$^{1/2}$) when P_{in} is 1 mW, and m_y is just 14ng. The gyroscope design proposed herein holds substantial promise for application in high-precision angular vibration measurements.

Future work will focus on experimental validation and potential applications in fields such as inertial navigation, geophysical exploration, and structural health monitoring where high angular precision is required.

Author Contributions: Writing—original draft preparation, software, conceptualization J.N.A.H.; review and editing, W.H.; review X.Y., S.Z. and D.C.; supervision, visualization, review and validation, G.W. and Y.H. All authors have read and agreed to the published version of the manuscript.

Funding: This work was supported in part by the National Natural Science Foundation of China under Grants 62371106, 61971113, and U2230206, in part by the National Key R&D Program under Grants 2018YFB1802102, and 2018AAA0103203, in part by the Guangdong Provincial Research and Development Plan in Key Areas under Grants 2019B010141001, and 2019B010142001, in part by the Joint Fund of ZF and Ministry of Education (Grant No. 8091B022126), in part by the Sichuan Provincial Science and Technology Planning Program of China under Grants 2021YFG0013, 2021YFH0133, 2022YFG0230, and 2023YFG0040, in part by Innovation Ability Construction Project for Sichuan Provincial Engineering Research Center of Communication Technology for Intelligent IoT (2303-510109-04-03-318020).

Institutional Review Board Statement: Not applicable.

Informed Consent Statement: Not applicable.

Data Availability Statement: Data underlying the results presented in this paper are available from the authors upon reasonable request.

Conflicts of Interest: The authors declare no conflicts of interest.

References

1. Addabbo, T.; Fort, A.; Biondi, R.; Cioncolini, S.; Mugnaini, M.; Rocchi, S.; Vignoli, V. Measurement of angular vibrations in rotating shafts: Effects of the measurement setup nonidealities. *IEEE Trans. Instrum. Meas.* **2013**, *62*, 532–543. [CrossRef]
2. Yang, M.; Liu, Z.; Wang, Y.; Cai, C.; Yang, J. Monocular vision-based multi-parameter dynamic calibration method used for the low-frequency linear and angular vibration sensors. *IEEE Trans. Ind. Electron.* **2022**, *70*, 5365–5374. [CrossRef]
3. Li, A.; Jing, Z.; Liu, Q.; Liu, Y.; Cheung, Y.; Zhang, Y.; Zhou, D.P.; Peng, W. IFOG Based on Rhombic Optical Path Difference Bias Configuration for High-Frequency Angular Vibration Measurement. *IEEE Sens. J.* **2022**, *22*, 16892–16897. [CrossRef]
4. Wang, Y.; Cao, R.; Li, C.; Dean, R.N. Concepts, Roadmaps and Challenges of Ovenized MEMS Gyroscopes: A Review. *IEEE Sens. J.* **2021**, *21*, 92–119. [CrossRef]
5. Larkin, K.; Ghommem, M.; Serrano, M.; Abdelkefi, A. A review on vibrating beam-based micro/nano-gyroscopes. *Microsyst. Technol.* **2021**, *27*, 4157–4181. [CrossRef]
6. Ren, X.; Zhou, X.; Yu, S.; Wu, X.; Xiao, D. Frequency-Modulated MEMS Gyroscopes: A review. *IEEE Sens. J.* **2021**, *21*, 26426–26446. [CrossRef]
7. Li, Z.; Gao, S.; Jin, L.; Liu, H.; Niu, S. Micromachined vibrating ring gyroscope architecture with high-linearity, low quadrature error and improved mode ordering. *Sensors* **2020**, *20*, 4327. [CrossRef]
8. Liu, X.S.; Yang, Z.C.; Chi, X.Z.; Cui, J.; Ding, H.T.; Guo, Z.Y.; Lv, B.; Lin, L.T.; Zhao, Q.C.; Yan, G.Z. A doubly decoupled lateral axis micromachined gyroscope. *Sensors Actuators, A Phys.* **2009**, *154*, 218–223. [CrossRef]
9. Xie, J.; Shen, Q.; Hao, Y.; Chang, H.; Yuan, W. Design, fabrication and characterization of a low-noise Z-axis micromachined gyroscope. *Microsyst. Technol.* **2015**, *21*, 625–630. [CrossRef]
10. Trusov, A.A.; Prikhodko, I.P.; Zotov, S.A.; Shkel, A.M. Low-dissipation silicon tuning fork gyroscopes for rate and whole angle measurements. *IEEE Sens. J.* **2011**, *11*, 2763–2770. [CrossRef]
11. Zhang, T.; Zhou, B.; Yin, P.; Chen, Z.; Zhang, R. Optimal design of a center support quadruple mass gyroscope (CSQMG). *Sensors* **2016**, *16*, 613. [CrossRef] [PubMed]
12. Sheikhaleh, A.; Jafari, K.; Abedi, K. Design and Analysis of a Novel MOEMS Gyroscope Using an Electrostatic Comb-Drive Actuator and an Optical Sensing System. *IEEE Sens. J.* **2019**, *19*, 144–150. [CrossRef]
13. Trigona, C.; Ando, B.; Baglio, S. Fabrication and Characterization of an MOEMS Gyroscope Based on Photonic Bandgap Materials. *IEEE Trans. Instrum. Meas.* **2016**, *65*, 2840–2850. [CrossRef]
14. Xia, D.; Zhang, B.; Wu, H.; Wu, T. Optimization and fabrication of an moems gyroscope based on a wgm resonator. *Sensors* **2020**, *20*, 7264. [CrossRef] [PubMed]
15. Yang, L.; Zhao, S.; Geng, J.; Xue, B.; Zhang, Y. Sensitivity enhancement of micro-optical gyro with photonic crystal. *Chin. Phys. B* **2021**, *30*, 044208. [CrossRef]
16. Zhang, H.; Peng, M.; Xu, X.W.; Jing, H. Anti- -symmetric Kerr gyroscope. *Chin. Phys. B* **2022**, *31*, 14215. [CrossRef]
17. Kippenberg, T.J.; Vahala, K.J. Cavity optomechanics: Back-action at the mesoscale. *Science* **2008**, *321*, 1172–1176. [CrossRef]
18. Aspelmeyer, M.; Kippenberg, T.J.; Marquardt, F. Cavity optomechanics. *Rev. Mod. Phys.* **2014**, *86*, 1391–1452. [CrossRef]
19. Abbott, B.P.; Abbott, R.; Abbott, T.D.; Abernathy, M.R.; Acernese, F.; Ackley, K.; Adams, C.; Adams, T.; Addesso, P.; Adhikari, R.X.; et al. Observation of gravitational waves from a binary black hole merger. *Phys. Rev. Lett.* **2016**, *116*, 061102. [CrossRef]
20. Forstner, S.; Knittel, J.; Sheridan, E.; Swaim, J.D.; Rubinsztein-Dunlop, H.; Bowen, W.P. Sensitivity and performance of cavity optomechanical field sensors. *Photonic Sens.* **2012**, *2*, 259–270. [CrossRef]
21. Gavartin, E.; Verlot, P.; Kippenberg, T.J. A hybrid on-chip optomechanical transducer for ultrasensitive force measurements. *Nat. Nanotechnol.* **2012**, *7*, 509–514. [CrossRef] [PubMed]
22. Huang, Y.; Flor Flores, J.G.; Li, Y.; Wang, W.; Wang, D.; Goldberg, N.; Zheng, J.; Yu, M.; Lu, M.; Kutzer, M.; et al. A Chip-Scale Oscillation-Mode Optomechanical Inertial Sensor Near the Thermodynamical Limits. *Laser Photonics Rev.* **2020**, *14*, 1800329. [CrossRef]
23. Davuluri, S.; Li, K.; Li, Y. Gyroscope with two-dimensional optomechanical mirror. *New J. Phys.* **2017**, *19*, 113004. [CrossRef]
24. Li, K.; Davuluri, S.; Li, Y. Improving optomechanical gyroscopes by coherent quantum noise cancellation processing. *Sci. China Phys. Mech. Astron.* **2018**, *61*. [CrossRef]
25. Li, G.; Lu, X.-M.; Wang, X.; Xin, J.; Li, X. Optomechanical gyroscope simultaneously estimating the position of the rotation axis. *J. Opt. Soc. Am. B* **2022**, *39*, 98. [CrossRef]

26. Madugani, R.; Yang, Y.; Ward, J.M.; Le, V.H.; Nic Chormaic, S. Optomechanical transduction and characterization of a silica microsphere pendulum via evanescent light. *Appl. Phys. Lett.* **2015**, *106*, 3–7. [CrossRef]
27. Haus, H.A. Waves and Fields in Optoelectronics. *Prentice-Hall Englewood Cliffs* **1984**, *32*, 748.
28. Rasoloniaina, A.; Huet, V.; Thual, M.; Balac, S.; Féron, P.; Dumeige, Y. Analysis of third-order nonlinearity effects in very high-Q WGM resonator cavity ringdown spectroscopy. *J. Opt. Soc. Am. B* **2015**, *32*, 370. [CrossRef]
29. Acar, C.; Shkel, A. *MEMS Vibratory Gyroscopes Structural Approaches to Improve Robustness*; Springer: New York, NY, USA, 2009; Volume 27.
30. Krause, A.G.; Winger, M.; Blasius, T.D.; Lin, Q.; Painter, O. A high-resolution microchip optomechanical accelerometer. *Nat. Photonics* **2012**, *6*, 768–772. [CrossRef]
31. Oskooi, A.F.; Roundy, D.; Ibanescu, M.; Bermel, P.; Joannopoulos, J.D.; Johnson, S.G. Meep: A flexible free-software package for electromagnetic simulations by the FDTD method. *Comput. Phys. Commun.* **2010**, *181*, 687–702. [CrossRef]
32. Djurić, Z. Mechanisms of noise sources in microelectromechanical systems. *Microelectron. Reliab.* **2000**, *40*, 919–932. [CrossRef]
33. Blasius, T.D. Optomechanical Inertial Sensors and Feedback Cooling. 2016, 2016. Ph.D. Thesis, California Institute of Technology, Pasadena, CA, USA, 2016. [CrossRef]
34. Baraillon, J.; Taurel, B.; Labeye, P.; Duraffourg, L. Linear analytical approach to dispersive, external dissipative, and intrinsic dissipative couplings in optomechanical systems. *Phys. Rev. A* **2020**, *102*, 33509. [CrossRef]
35. Thompson, J.D.; Zwickl, B.M.; Jayich, A.M.; Marquardt, F.; Girvin, S.M.; Harris, J.G.E. Strong dispersive coupling of a high-finesse cavity to a micromechanical membrane. *Nature* **2008**, *452*, 72–75. [CrossRef] [PubMed]
36. Clerk, A.A. Optomechanics and Quantum Measurement. *Quantum Optomech. Nanomech.* **2020**, 183–236. [CrossRef]
37. Kim, M.; Cho, B.; Lee, H.; Yoon, T.; Lee, B. Implementation of Hemispherical Resonator Gyroscope with 3 × 3 Optical Interferometers for Analysis of Resonator Asymmetry. *Sensors* **2022**, *22*, 1971. [CrossRef] [PubMed]
38. Zhao, W.; Yang, H.; Liu, F.; Su, Y.; Li, C. High sensitivity rate-integrating hemispherical resonator gyroscope with dead area compensation for damping asymmetry. *Sci. Rep.* **2021**, *11*, 2195. [CrossRef] [PubMed]
39. Pistorio, F.; Saleem, M.M.; Somà, A. A dual-mass resonant mems gyroscope design with electrostatic tuning for frequency mismatch compensation. *Appl. Sci.* **2021**, *11*, 1129. [CrossRef]
40. Zwerger, W. Cavity-assisted backaction cooling of mechanical resonators. *New J. Phys.* **2008**, *10*, 095007. [CrossRef]
41. Acar, C.; Schofield, A.R.; Trusov, A.A.; Costlow, L.E.; Shkel, A.M. Environmentally robust MEMS vibratory gyroscopes for automotive applications. *IEEE Sens. J.* **2009**, *9*, 1895–1906. [CrossRef]
42. Bukhari, S.A.R.; Saleem, M.M.; Khan, U.S.; Hamza, A.; Iqbal, J.; Shakoor, R.I. microfabrication process-driven design, FEM analysis and system modeling of 3-DoF drive mode and 2-DoF sense mode thermally stable non-resonant MEMS gyroscope. *Micromachines* **2020**, *11*, 862. [CrossRef]
43. Din, H.; Iqbal, F.; Lee, B. Design approach for reducing cross-axis sensitivity in a single-drive multi-axis mems gyroscope. *Micromachines* **2021**, *12*, 902. [CrossRef]